Twin-structured Graphene Metamaterials with Anomalous Mechanical Properties

Zaishan Lin [1, 2,†], Jiaqi Dong[3,†], Xin Wang [1, 2,†], Qitao Huang[4,†], Xi Shen[5], Minglong Yang[1, 2], Xianxian Sun[1, 2], Ye Yuan[6], Shasha Wang[1, 2], Yuanhao Ning[1, 2], Shuang Yang[1, 2], Weilong Yin[1, 2], Menglin Li[7], Yiwei Sun[8], Qiangqiang Zhang[3*], Yibin Li[1, 2, 6 *]

[1]National Key Laboratory of Science and Technology on Advanced Composites in Special Environments, Harbin Institute of Technology, Harbin 150080, P. R. China

[2]Center for Composite Materials and Structures, Harbin Institute of Technology, Harbin 150080, P. R. China

[3]College of Civil Engineering and Mechanics, Key Laboratory of Mechanics on Disaster and Environment in Western China and the Ministry of Education of China, Lanzhou University, Lanzhou 730000, P. R. China

[4]School of Mechanical Engineering, Harbin Institute of Technology, Harbin 150080, P. R. China

[5]Department of Aeronautical and Aviation Engineering, The Hong Kong Polytechnic University, Hung Hom, Hong Kong SAR, China

[6]School of Materials Science and Engineering, Beihang University, Beijing 100191, P. R. China

[7] Key Laboratory of Energy Thermal Conversion and Control of Ministry of Education, School of Energy and Environment, Southeast University, Nanjing 210096, P. R. China

[8] School of Materials Science and Engineering, School of Energy and Environment, Southeast University, Nanjing 210096, P. R. China

This article has been accepted for publication and undergone full peer review but has not been through the copyediting, typesetting, pagination and proofreading process, which may lead to differences between this version and the Version of Record. Please cite this article as doi: 10.1002/adma.202200444.

E-mail: liyibin@buaa.edu.cn (Y. Li) and zhangqq@lzu.edu.cn (Q. Zhang)

Keywords: graphene metamaterials, twin structure, Poisson's ratio, anomalous mechanical properties

Abstract: Typically, solid materials exhibit transverse contraction in response to stretching in the orthogonal direction and transverse expansion under compression conditions. However, when flexible graphene nanosheets are assembled into three-dimensional (3D) porous architecture, the orientation arrangement delivered directional deformation of micro-nanosheets may induce anomalous mechanical properties. In this study, a 3D hierarchical graphene metamaterial (GTM) with twin-structured morphologies is assembled by manipulating the temperature gradient for the ice growth during *in situ* freeze-casting procedures. GTM has demonstrated anomalous anisotropic compression performance with programable Poisson's ratios (PRs) and improved mechanical properties (*e.g.*, elasticity, strength, modulus and fatigue resistance) along different directions. Owing to the designed three-phase deformation (elastic bending, out-of-plane buckling, and large deflection) of two-dimensional graphene sheets as basic elements in the microscale, the twin-structure GTM delivers distinctive characteristics of compressive curves with an apparent stress plateau and follows a strengthening tendency. This multiscale deformation behavior facilitates the enhancement of energy loss coefficient under large compression. In addition, a finite element theory based numerical model is established to optimize the structural design, and validate the multiscale tunable PR mechanism and oriented structural evolution. The mechanical and thermal applications of GTM indicate that the rational manipulation-driven design of meta-structures paves the way for exploring graphene-based multifunctional materials with anomalous properties.

1. Introduction

Materials generally exhibit transverse contraction in response to stretching in the orthogonal direction and transverse expansion under compression conditions.[1] The deformation performance in the transverse direction is governed by material attribution, referred to as the engineering Poisson's ratio (PR), ν_{ij}, which is defined as $\nu_{ij} = -\varepsilon_{ii}/\varepsilon_{jj}$.[2] PRs of most naturally existing or artificial materials are positive, with a few exceptions, such as 0.5 for rubber, 0.1–0.4 for polymer foam, and nearly zero for cork.[2–5] Theoretically, to ensure a positive value for the shear modulus ($G= \frac{E}{2(1+\nu)}$) and volume modulus ($K = \frac{E}{3(1-2\nu)}$), the permissible PR ranges from −1.0 to 0.5 based on the elasticity theory of solid mechanics.[6,7]

The as-reported functional materials with different PRs have demonstrated entirely different deformation behaviors, such as global contraction or expansion.[8–11] For instance, the negative PR (NPR) effect causes materials to display a distinct mechanical constitutive model with the anomalous three-stage characteristic of strain vs. stress curves, including linear elasticity, stress plateau, and nonlinear hardening stage.[12–14] NPR materials are expected to significantly improve the mechanical properties by ensuring larger compressive strength, better elasticity, more robust structure, and higher fatigue resistance.[2,15–18] Fundamentally, the deformation performance of porous materials is dominated by the alignment and orientation of basic micro-elements. Therefore, the related global mechanical properties and PR performance can be modulated using a microstructural multiscale design and artificial manufacturing process.[18,19]

Three-dimensional (3D) lightweight graphene monoliths with high electrical conductivities, low thermal conductivities, and large energy dissipation capacities have demonstrated their potential as sensors,[20,21] thermal barriers,[22,23] conductors, dampers [24] and functional network in advanced composites.[25] To maintain the stability of these reported extraordinary performances, the priority is to warrant the structural robustness of 3D graphene monoliths under inevitable deformation induced by either mechanical compression or thermal excitation in diverse applications.[20,21,26] Several researchers have attempted to fabricate 3D graphene monoliths with NPR to improve the mechanical properties using a rationally designed architecture.[27] Previously reported 3D graphene monoliths primarily focus on isotropic performance derived from symmetric structures.[28–30] However, the materials predominantly undergo anisotropic loading, which manifests as complex stress and strain distributions. Although the anisotropic design of microstructures with unique patterns can ensure effective programmable regulation of mechanical properties, such as twin crystals rather than long-period ordered stacking structures, it has not been sufficiently investigated in 3D graphene monoliths.

In this study, a 3D twin-structured graphene metamaterial (GTM) is constructed with two-dimensional (2D) graphene sheets, which serve as basic assembling units in the directional freeze-casting manipulation. Based on the elastic deformation (bending or buckling) in a specifically designed orientation of 2D graphene sheets in the microscale, the developed GTM demonstrates programmable mechanical properties, including anisotropic compression behaviors corresponding to different PRs in different directions. A numerical model was established to reveal the correlation mechanism between global deformation behavior and microstructural evolution under different loading transfer formats. This validates that oriented bending followed by elastic buckling of the main branches in the twin structure induces the anisotropic deformation and high resilience of GTM. The distinctive mechanical properties and thermal conductivity corresponding to different internetworks along three orthogonal directions further demonstrate the promising applications of GTM as a potential candidate for dampers, thermal insulators, and functional composites (*e.g.*, metal, polymer or ceramic matrixes).

2. Results and Discussion

2.1. Design and Fabrication of GTM

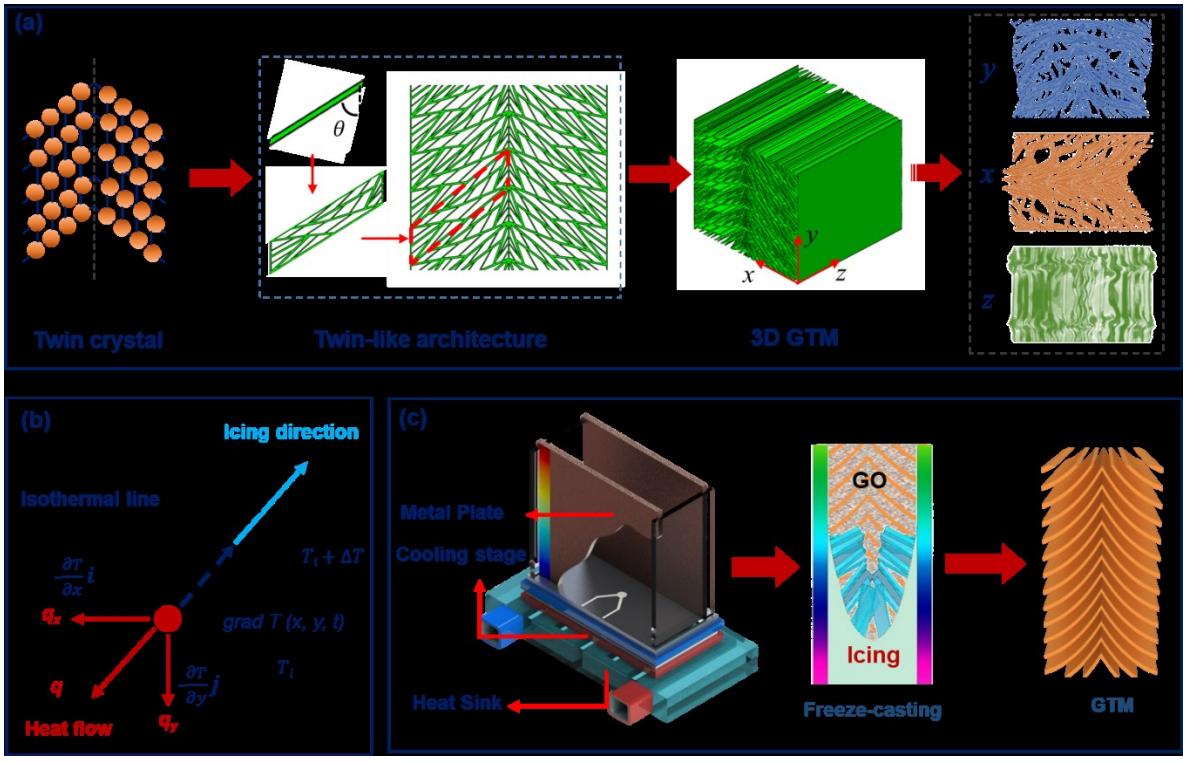

Figure 1. (a) The multiscale design of a twin-structured graphene metamaterial (GTM). The anisotropic deformation behaviors of three compressive schemes along *y*-, *x*-, and *z*-axes. (b) The theoretical schema of icing growth orientation under different freezing process-induced temperature gradients. (c) Fabrication of GTM via oriented freezing and post-processing involvement of drying and thermal reduction.

Owing to the symmetric alignment of atoms in the microstructure rather than the long-period stacking structure, twin crystals normally exhibit unique deformation characteristics and improved mechanical properties, such as compression strength, fracture toughness, and fatigue resistance. This increases the potential of applying twin crystals in multiple fields.[31] Inspired by the excellent performance of crystals with twin structure, we designed a hierarchically ordered meta-architecture with a symmetric twin-like pattern in the *x*–*y* plane constructed from graphene sheets of a few layers as basic cell walls at a certain orientation angle of θ (**Figure 1a**). The finite element numerical simulation conducted by Abaqus 6.10 indicates that GTM exhibits entirely anisotropic mechanical properties with programmable deformation behaviors under unidirectional compression, such as symmetric NPR, antisymmetric positive PR (PPR)–NPR, and near-zero PR performances along the y-, x-, and z-axes, respectively. This can be attributed to the unique orientation characteristics of the multiscale twin-structure.

To obtain the designed twin-patterned structures, we propose a directional freeze-casting method for constructing a GTM from a graphene oxide (GO) aqueous precursor. Theoretically, the phase transition of materials is physically accompanied by an endothermic or exothermic phenomenon.[32] As depicted in **Figure 1b**, heat energy generally flows from a higher- to lower-temperature regions among the isothermal lines at the moving boundary of the water-to-ice phase transition. This reveals that the freezing process of the GO aqueous precursor can be manipulated by controlling the heat transfer routines. According to Fourier's law, the temperature gradient is antiparallel to the direction of the heat flux, which intrinsically dominates the growth orientation (θ) of ice crystals (**Equation 1** and **2**).[33] Consequently, the twin-patterned microstructure of GTM can be created accurately through a directional freeze-casting process under the rational manipulation of the temperature gradient in two orthogonal directions. The structural orientation can be designed using the critical parameter θ, as indicated in **Equation 3**.

$$\text{grad } T(x, y, t) = \frac{\partial T}{\partial x}\boldsymbol{i} + \frac{\partial T}{\partial y}\boldsymbol{j} \qquad (1)$$

$$q = -\lambda \text{ grad } T(x, y, t) = -\lambda\left(\frac{\partial T}{\partial x} i + \frac{\partial T}{\partial y} j\right) \quad (2)$$

$$\theta = \sin^{-1}\left(\frac{\left|\frac{\partial T}{\partial x}\right|}{\sqrt{\left(\frac{\partial T}{\partial x}\right)^2 + \left(\frac{\partial T}{\partial y}\right)^2}}\right) \quad (3)$$

where T (x, y, t) denotes the temperature field (°C), grad T indicates the temperature gradient (°C mm^{-1}), λ represents the thermal conductivity (W m^{-1}·K^{-1}), $\boldsymbol{q}$ denotes the heat flow density (W m^{-2}), and ϑ indicates the oblique angle of both the ice growth and graphene sheet orientation (°).

Figure 1c and **S1** depict the schematic and actual freeze-casting process, respectively. The device comprises lateral metal plates (stainless steel (SS), aluminum alloy (AA), copper (Cu)) and a bottom cooling stage (−25 °C). It was established for a controlled construction of GTM under a dual temperature gradient-derived directional freezing process along two orthogonal directions (x–y plane). GTM with the designed twin microstructure was prepared through directional freeze-casting and subsequent processes involved *in situ* drying and chemical reduction (**Figure S2a–c**). During this process, the GO sheets were orderly aligned as basic units into a twin-oriented structure under ice crystal-induced assembly. The anisotropic characteristics (pattern feature, sheet orientation, and pore size) of the GTM structure in the three directions can be controlled by different freezing pathways. More details of the GTM fabrication process are provided in the **Supporting Information**.

2.2. Microstructural Characterizations of GTM

As depicted in **Figure 2a**, the freeze-casting device with different lateral metal plates exhibits different freezing transitions of the GO precursor based on the diverse temperature distribution. Ice crystals develop along the normal direction of the isothermal interface during liquid-to-solid phase changes. The freezing plates with a higher thermal conductivity, SS: 15.1 W m^{-1}·K^{-1} > AA: 130.0 W m^{-1}·K^{-1} > Cu: 386.4 W m^{-1}·K^{-1}, reveal that a faster cooling procedure results in larger curvatures of isothermal surface (solution-to-ice boundary) (**Figure S3**). This enables optimization of the icing orientation by manipulating the heat flow between the vertical and horizontal directions based on the compromised regulation of the dual temperature gradient.

As presented in **Figure 2b** and **c** and **Table 1**, the temperature changes ($\frac{\partial T}{\partial x}$ and $\frac{\partial T}{\partial y}$, $^{\circ}\mathrm{C/mm}$) and freezing direction (ϑ, °) along the x- and y-axes are extracted from the profile curves of the temperature contours in the x–y plane. The freezing process significantly relies on the thermal diffusion capacity of the lateral metal plate (SS < AA < Cu). The orientation of the ice growth is strongly dominated by either bottom-up cooling for the SS device ($\frac{\partial T}{\partial x} = 0.42 \gg \frac{\partial T}{\partial y} = 0.14$) or

lateral-to-inside freezing for the Cu device ($\frac{\partial T}{\partial x} = 0.07 \ll \frac{\partial T}{\partial y}$ =0.35). Conversely, the AA device realizes compromised freezing between the two orthogonal directions ($\frac{\partial T}{\partial x} = \frac{\partial T}{\partial y} = 0.27$).

Figure 2d–f indicate that the GTM structure presents the expected anisotropic characteristics as a symmetrical twin pattern in the *x*–*y* plane (front), whereas a uniform porous-lamellar internetwork is observed in the *y*–*z* (lateral) and *x*–*z* planes (top) (**Figure S4–5**). Owing to the different orientations of ice growth, the GO sheets were squeezed among the interfaces of ice crystals to assemble into a 3D twin-like architecture. The corresponding angles (ϑ) between the major cell wall and the symmetric plane were 18.4 °±0.92, 45 °±2.25, and 78.7 °±3.93 for GTM-SS, -AA, and -Cu, respectively. As the size of the ice nucleus significantly relies on the temperature variation, a lower temperature facilitates uniform nucleation and growth of ice crystals with finer diameters.[34] Statistically, corresponding to different freezing plates of SS, AA, and Cu, GTM exhibits the totally different pore dimensions of the hierarchical microstructure as depicted in **Figure 2g**, **h**, and **i**, respectively. For instance, the pore dimensions of GTM–SS clusters at 150 to 400 μm (**Figure 2j**), while GTM–AA demonstrates the typical normal distribution feature from 200 to 875 μm with average size about 400 μm (**Figure 2k**). Comparatively, the pore dimensions for GTM–Cu separately distributes at two intervals as 100 to 300 μm and 800 to 1300 μm. The diverse distribution of pore dimension being less than 1 μm is further demonstrated in **Figure S6** with the BET surface area as large as 7.48±043, 7.70±0.34 and 8.49±0.24 $m^2 g^{-1}$ for GTM-SS, -AA, and -Cu, respectively.

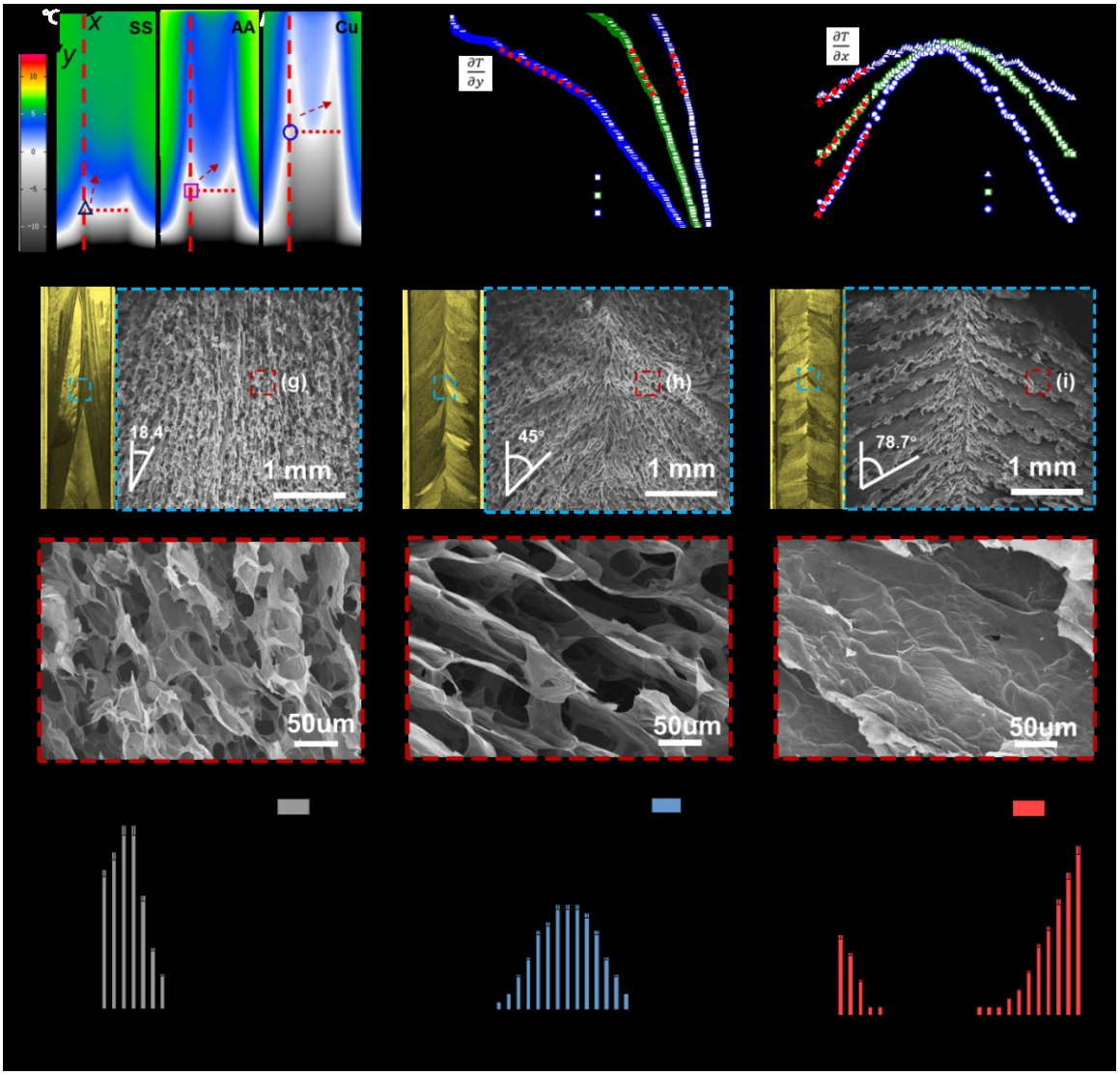

Figure 2. Structural characterizations of graphene metamaterial (GTM). (a) Infrared mappings in the *x*–*y* plane of graphene oxide (GO) precursor within the device during freezing at 30 min. The changing temperature profiles along (b) *x*- and (c) *y*-axes. The twin patterned structure and oriented graphene sheet of GTM generated by different freezing plates, namely (d) stainless steel (SS), (e) aluminum alloy (AA), and (f) copper (Cu). The microstructural evolution from porous to lamellar morphologies corresponding to GTM- (g) SS, (h) AA, and (i) Cu. The statistics of pore dimensions from SEM observation to GTM- (j) SS, (k) AA, and (l) Cu.

Table 1 Temperature gradient and icing orientation for different freezing formats.

Index	GTM-SS	GTM-AA	GTM-Cu
$\frac{\partial T}{\partial y}$ [°C/mm]	0.42±0.021	0.27±0.014	0.07±0.004

$\frac{\partial T}{\partial x}$ [°C/mm]	0.14±0.007	0.27±0.014	0.35±0.018
θ [°]	18.4±0.92	45.0±2.25	78.7±3.93

Furthermore, the change in the chemical component during GTM fabrication is characterized by an X-ray diffraction (XRD) pattern. As depicted in **Figure S2d**, the oxide GTM exhibits an apparent peak at 11.1 °,[35] which originates from GO with an interlayer spacing of 8.6 Å for the (002) plane. After using $N_2H_4{\cdot}H_2O$ for the chemical reduction, the shifted peak at 22.4 ° indicates significant graphitization of reduced GO with an interlayer spacing of 3.9 Å. The removal of oxygenated functional groups implies the effective recovery of π–π conjugate domains, which is further validated by the intensified G-band of the Raman spectrum as an indication of the symmetry and order of the reduced GO lattice (**Figure S2e**).

2.3. Programmable Properties of GTM

The twin structure is known to result in an anomalous performance beyond that of the traditional system owing to the unique response to external loads.[31] As depicted in **Figure 3a**, GTM exhibits a significant NPR effect, with the transverse contraction appearing along the *x*-axis under uniaxial compression in the *y*-direction. Furthermore, ε_x linearly depends on ε_y ranging from 0 to 50% with a NPR (ν_{xy}) of −0.2 (**Figure 3b**). The numerical simulation indicates that the macroscopic NPR behavior of GTM is symmetrically driven by the reentrant deformation of the twin structure (**Figure 3c**). Additionally, as depicted in **Figure S7**, elastic slip regions formed in the twin structure facilitate the compression–shear coupling deformation of basic cells at the multiscale. Fundamentally, the highly elastic compressibility of GTM originates from the microscale dislocation slip oriented inward among the primary thicker walls (A–B and C–B) under the constraint of a symmetric plane. A lateral thinner wall (A–C) with more complex buckling modes, such as the S-shaped second-order mode, offers a larger internal resilience to overcome the van der Waals force among the micro-interfaces of graphene walls within the GTM at large compressive strains.

As depicted in **Figure 3d** and **e**, the GTM displays distinguished deforming features as antisymmetric PR performance with the right contraction but left expansion. However, the values of PR (ν_{yx}) are −0.2 and 0.14 corresponding to the *y*–*z* plane at right and left sides, respectively. In the microstructure, the horizontal cell walls (D–E) adjacent to the twin boundaries exhibit directional immigration toward the left side, which induces an anti-symmetrically oriented deformation along the *x*-axis. The other walls are squished together under compression–bending coupling deformation (**Figure S8**), and the resilience force for GTM recovery mostly affords by main thicker walls (D–F and

D–G). When GTM is compressed along the *x*-axis (**Figure 3g**), neither expanding or shrinking deformation occurs in the transverse direction, which indicates a near-zero PR ($\nu_{zx} \approx 0$) (**Figure 3h** and **i**). This is because the vertically aligned graphene cell wall generally exhibits pure compression-induced out-of-plane bending and buckling without a specific orientation. Overall, among the three different loading schemes depicted in Figure 3a, d, and g, the basic micro-wall typically exhibits three-stage deformation features, such as out-of-plane deformation, buckling, and large deflection. This affects the macroscopic mechanical properties (*e.g.*, elasticity, modulus and fatigue resistance) with a distinct tendency of the strain vs. stress curves.

Figure 4a–c and **S9** illustrate the anisotropic mechanical properties exhibited by GTM. The compression curves of strain vs. stress demonstrate the typical three-stage nonlinear characteristics of lightweight monoliths, namely the linear elasticity, stress plateau, and solidification, enabling a superplastic capacity with recoverable compression strain of over 50%. Compared with three different GTM, the twin-ordered structure along y-axis further enhances the strength from 2.3±0.115 kPa (GTM-SS) to 3.4±0.170 kPa (GTM-Cu) during compression along z-axis due to the increase of graphene walls stability. According to the numerical modeling depicted in Figure 1a, the macroscopic super-elasticity of GTM originates from elastic buckling caused by a large deflection and small strain of graphene cell walls at the microscale. This indicates that directional freezing strategy-derived structural manipulation can potentially regulate the mechanical properties of GTMs.

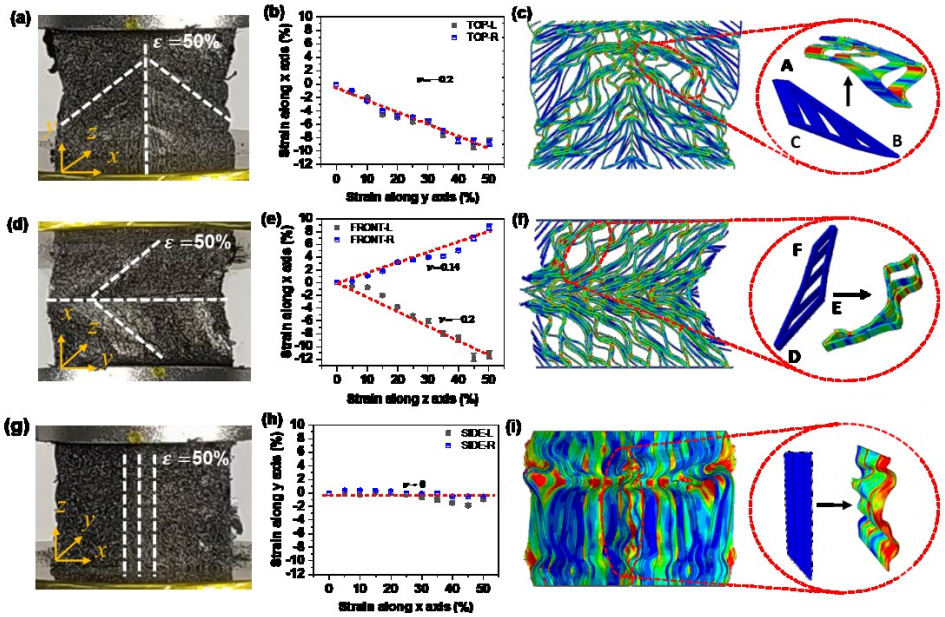

Figure 3. Different deforming behaviors of the graphene metamaterial (GTM). (a–c) The symmetrically negative Poisson's ratio (NPR) along the *y*-axis. (d–f) The antisymmetric PR along the

x-axis (positive and negative PRs on the left and right side, respectively.) (g–i) The near-zero PR along the *z*-axis.

Both **Table 2** and **3** list the results of maximum stress (50% strain) and Young's modulus (1.2% strain) of GTMs fabricated using different freezing formats. The vertically aligned structure produced by SS exhibits the highest compression strength of 3.6±0.180 kPa along the *y*–axis (top view) at a compressive strain of 50%. The maximum Young's modulus at linear–elastic stage (1.2% strain) is about 31±1.550 kPa. In comparison, these two parameters for twin–structured GTM are much higher than that of some randomly ordered 3D graphene monoliths. [28] By contrast, GTM-Cu exhibits nearly antithetical performance with the lowest stress and Young's modulus of 1.9±.095 and 11.7±0.585 kPa. This is because vertically oriented cell walls predominantly exhibit out-of-plane bending with higher critical stress rather than a compacting deformation of the lamellar structure or disordered network (**Figure 4d**). [28] **Equation 4** is obtained by considering the theory of thin-wall buckling; the calculated critical stress (σ_{cr}) of the vertical wall ($\beta = 2$) is substantially higher than that of either the inclined ($\beta = 2cos\theta$) or horizontal wall ($\beta \to 0$) under vertical loading.

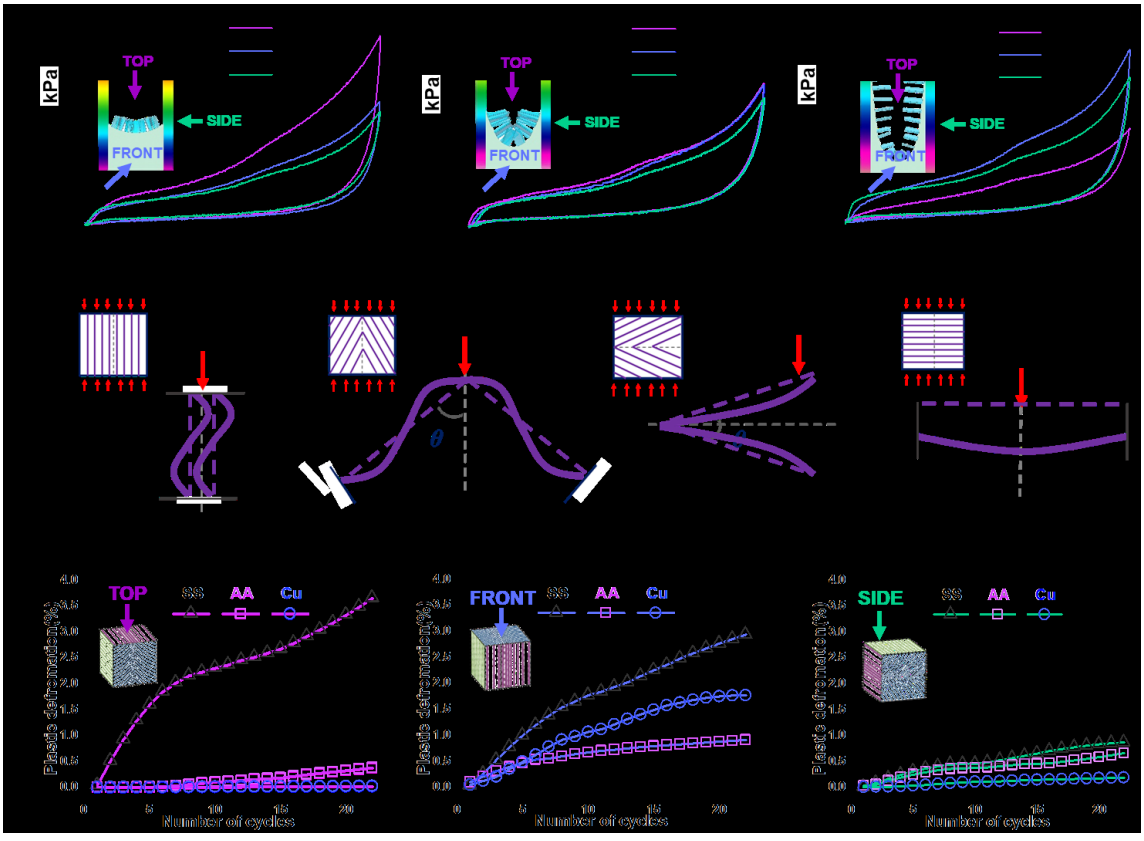

Figure 4. Mechanical properties of the graphene metamaterial (GTM). The compression curves of strain vs. stress along different directions for samples produced in freezing devices of (a) stainless steel (SS), (b) aluminum alloy (AA), and (c) copper (Cu). (d) The comparative buckling modes for

differently oriented cell walls at the microscale. The residual plastic deformations under cyclic compression along the (e) *x*-, (f) *z*-, and (g) *y*-axes for a sample fabricated using three different freezing devices.

Additionally, owing to the positive dependence of the critical stress (σ_{cr}) on $\sin\theta$, the maximum stress along the *x*-axis (side view) increases from 2.1±0.105 (GTM-SS) to 2.9±0.145 kPa (GTM-Cu) with the increase of θ from 18.4±0.92 to 78.7±3.93°. Unlike the similar mechanical properties of GTM-SS and -AA along either the *x*- or *z*-axis, the maximum stress and Young's modulus in the GTM-Cu are the largest (2.9±0.145 and 30±1.500 kPa) along the *z*-axis because of the hierarchical arch structure in the *x*–*z* plane (top view) (**Figure S6a–c**). Furthermore, as illustrated in **Figure 4e–g**, the plastic deformation is less than 0.5% for GTM with θ > 45 ° during 20 cyclic compressions along the *y*-axis, whereas the vertically aligned structure in the GTM-AA exhibits lower robustness with a plastic deformation as large as 3.8%. The apparent twin structure enables a significant improvement in structural fatigue resistance by regulating the multiscale deformation behaviors and internal stress distributions.

Table 2. Maximum stress at a strain of 50% for the GTM fabricated using different freezing styles.

Freezing style	Compression strength at the top (*x*–*z* plane) [kPa]	Compression strength at the front (*x*–*y* plane) [kPa]	Compression strength at the side (*y*–*z* plane) [kPa]
SS	3.6±0.180	2.3±0.115	2.1±0.105
AA	2.7±0.135	2.7±0.135	2.4±0.120
Cu	1.9±.095	3.4±0.170	2.9±0.145

Table 3. Young's modulus at a strain of 1.2% for the GTM fabricated using different freezing styles.

Freezing style	Compression strength at the top (*x*–*z* plane) [kPa]	Compression strength at the front (*x*–*y* plane) [kPa]	Compression strength at the side (*y*–*z* plane) [kPa]
SS	31.0±1.550	15.0±0.750	16.7±0.835
AA	25.0±1.250	15.8±0.790	21.7±1.085
Cu	11.7±0.585	16.7±0.835	30.0±1.500

$$\sigma_{cr} = \beta \frac{k}{12(1-\nu^2)} \frac{\pi^2 E t^2}{b^2} \quad (4)$$

where σ_{cr} denotes the critical stress of buckling deformation; β indicates the correction factor corresponding to different compression schemes; k represents the buckling coefficient; ν_{GW} and E_{GW} denote PR and Young's modulus of graphene wall (GW), respectively; and b and t indicate the width and thickness of the GW, respectively.

2.4. Potential Applications of GTM

Owing to the anisotropic structural characteristics of twin patterns created by different freeze-casting processes, GTM has distinctive mechanical properties. During compression along different directions, the GTM exhibits diverse hysteretic behavior with strain and stress, following a typical nonlinear dependence. This enables the use of GTM as a damper, ensuring sufficient capacity for energy absorption or vibration isolation during either quasistatic or dynamic deformation. As depicted in **Figure 5a**, the energy loss coefficient of the GTM ranges from 281.0±14.05 to 443.2±22.16 J m^{-3}, which is quantitively calculated using **Equation 5** considering the integral of the strain vs. stress curves in Figure 4a–c. This reveals that twin-structured GTM has the larger energy dissipation capacity at strain of 50% than some other reported 3D graphene monoliths with randomly oriented structure. [28] Furthermore, the arch-like architecture along the *z*-axis in GTM-Cu and the vertically aligned structure along the *x*-axis in GTM-SS exhibit the highest energy dissipation owing to the higher buckling stress and larger deflection of the small cell wall (Figure 2d). The lamellar-oriented structures in GTM-Cu and -SS along the *x*- and *y*-axes, respectively, exhibit the lowest energy-dissipating capacities.

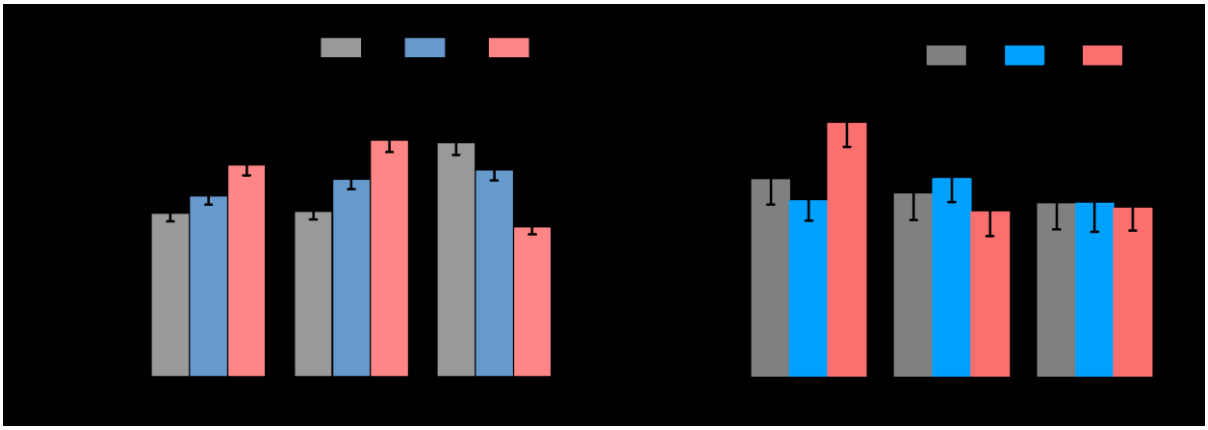

Figure 5. Investigation of graphene metamaterial (GTM) for potential applications. (a) The energy loss coefficient and (b) thermal conductivity of a sample fabricated using three different freezing

formats along the *x*-, *y*-, and *z*-axes, respectively. The symbol * indicates a significant difference between sample groups with P < 0.05.

$$\frac{W}{V} = \oint \sigma d\varepsilon \quad (5)$$

Typically, different networks in the microstructure reveal diverse pathways for energy transformation, which is viable to regulate thermal conductivity along different directions. As depicted in **Figure 5b**, the thermal conductivities under vacuum conditions for GTM-SS, -AA, and -Cu along the *y*-axis are 5.30±0.76, 5.73±0.67 and 4.78 ±0.70 mW m^{-1} K^{-1} corresponding to the orientation angle θ of 18.4 °±0.92, 45 °±2.25, and 78.7 °±3.93, respectively. It demonstrates the much more excellent thermal insulating ability rather than those of reported 3D graphene monoliths. [36] By contrast, the thermal conductive behavior exhibits the different dependence along the *x*- and *z*-axes rather than in the *y*-axis. The vertically oriented graphene sheet can directly conduct the in-plane heat through the shortest pathway, whereas the lamellar structure is dominated by the out-of-plane thermal transfer with a larger interface thermal resistance. As depicted in Figure 2, GTM-Cu also exhibits programmable thermal conductive capabilities of 4.78±0.70, 4.89±0. 65, and 7.33±0.67 mW m^{-1} K^{-1} along the *y*-, *z*-, and *x*-axes, respectively. Accordingly, the distinctive performance of the GTM on thermal conductivity is highly coincident with the specific orientation of the microstructure along different directions. The directional freeze-induced structural manipulation indicates an accessible method for the controllable design and fabrication of functional conductors or insulators with anisotropic thermal conductivity along corresponding directions.

3. Conclusion

In this study, we proposed a 3D twin-structured GTM constructed using quantitative manipulation of icing orientation and temperature gradient. Both experimental observations and numerical simulations reveal the evolution mechanism of multiscale hierarchical structures. The GTM demonstrates a unique dependence between compression curve (strain vs. stress) and deformation features of hierarchical structure. The twin-structure delivered orientation bending and elastic buckling formats of the cell wall were validated to generate anisotropic compression behavior and offer high resilience to enable super-elastic deformation. Furthermore, the twin-structured GTM exhibits a sequence of anomalous performance, including the programable PR effect (ν: −0.2 to +0.14), super-elasticity (elastic strain: ε_e > 50%), high fatigue resistance (plastic strain: ε_p < 0.5%),

large elastic modulus (E = 31 kPa) and ultra-low thermal conductivity (4.78±0.70 mW m^{-1} K^{-1}). Therefore, GTM can serve as an excellent candidate for a programmable damper, thermal insulator and functional composites beyond rational design and structural regulation-derived performance optimizations depending on different directions.

4. Experimental Section

Material Fabrication: The GTM was fabricated using an oriented freezing process under controllable manipulation of the temperature field using a directional freezing device. The expected temperature gradient was generated using lateral metal plates with different thermal conductivities. Under controlled ice growth, the 3D architecture was constructed using a GO aqueous precursor (concentration: 5 mg ml^{-1}) in the device with the temperature of the bottom cooling stage maintaining at −25 ℃. Subsequently, the frozen GO bulk was treated using a freeze-drying procedure to realize a 3D porous architecture with ice component sublimated completely. The twin-structured lightweight GTM was eventually obtained after chemical reduction using hydrazine hydrate at 95 °C for 24 h.

Numerical Calculation: The structural design of the GTM was implemented by finite element-based numerical methods using commercial software of Abaqus 6.1.0 with an ideal elastoplastic model. The analysis step sets as dynamic explicit process. The geometric size of macroscopic GTM model was 20×20×20 mm^3 with the thickness ratio between the thick and thin walls being 2:1. A 8-node linear hexahedron element (C3D8R) was selected as the basic unit. There are totally 621330 elements generated after meshed by the basic size of 0.5mm. The more details of parameter selection in simulation can be found in Supporting Information. The hierarchical structure was constructed with morphological similarity to the twin-patterned GTM. The compressive deformation behavior was calculated based on the large deflection theory of the thin wall, wherein the association mechanism of multiscale structural evolution was extracted during the vertical strain loading of up to 30%. General contact was implemented to avoid mutual impaling among walls during large deformations.

Characterization and Measurements: Scanning electron microscopy (SEM, Hitachi S-4800) was used to characterize the morphology of GTM. Powder XRD patterns were acquired on a Shimadzu XRD-7000s diffractometer. The reduction of the GO sheets was detected using Raman spectra determined using LabRAM HR800 (JY Horiba). The pore structure and BET surface area were

detected by a Micromeritics ASAP 2020 PLUS. The thermal conductivity was measured via a one-dimensional reference bar system modified from ASTM D-5470 under vacuum conditions as illustrated in Figure S10. [37] Fourier transform infrared spectroscopy was conducted by a TENSOR 27 machine (Bruker). The compression properties were measured using an Instron 5944 universal testing machine at a loading rate of 1 mm min^{-1}.

Supporting Information

Supporting Information is available online.

Acknowledgements

Z. S. Lin， J. Q. Dong, X. Wang and Q. T. Huang contributed equally. This work was supported by the Fund of Natural Science Foundation of China (Grant no. 51772063, 52073132). This work was also supported by the Fok Ying-Tong Education Foundation for Young Teachers in the Higher Education Institutions of China (Grant no. 171107), Science Fund for Distinguished Young Scholars of Gansu Province (Grant no. 18JR3RA263), Fundamental Research Funds for the Central Universities (Grant no. lzujbky-2020-ct05) and Natural Science Foundation of Jiangsu Province (Grant no. BK20200371).

Received: ((will be filled in by the editorial staff))
Revised: ((will be filled in by the editorial staff))
Published online: ((will be filled in by the editorial staff))

Conflict of Interest

The authors declare no conflict of interest.

References

[1] R. Lakes, Science **1987**, *235*, 1038.

[2] Y. Wu, N. Yi, L. Huang, T. Zhang, S. Fang, H. Chang, N. Li, J. Oh, J. A. Lee, M. Kozlov, A. C. Chipara, H. Terrones, P. Xiao, G. Long, Y. Huang, F. Zhang, L. Zhang, X. Lepro, C. Haines, M. D. Lima, N. P. Lopez, L. P. Rajukumar, A. L. Elias, S. Feng, S. J. Kim, N. T. Narayanan, P. M. Ajayan, M. Terrones, A. Aliev, P. Chu, Z. Zhang, R. H. Baughman, Y. Chen, *Nat. Commun.* **2015**, *6*, 1.

[3] Y. Si, X. Wang, L. Dou, J. Yu, B. Ding, *Sci. Adv.* **2018**, *4*, eaas8925.

[4] H. Lu, X. Zhang, W. G. Knauss, *Polym. Eng. Sci.* **1997**, *37*, 1053.

[5] G. N. Greaves, A. L. Greer, R. S. Lakes, T. Rouxel, *Nat. Mater.* **2011**, *10*, 823.

[6] R. Lakes, *Adv. Mater.* **1993**, *5*, 293.

[7] D. Chen, J. Yang, S. Kitipornchai, *Compos. Sci. Technol.* **2017**, *142*, 235.

[8] X. Xu, Q. Zhang, M. Hao, Y. Hu, Z. Lin, L. Peng, T. Wang, X. Ren, C. Wang, Z. Zhao, C. Wan, H. Fei, L. Wang, J. Zhu, H. Sun, W. Chen, T. Du, B. Deng, G. J. Cheng, I. Shakir, C. Dames, T. S. Fisher, X. Zhang, H. Li, Y. Huang, X. Duan, *Science* **2019**, *363*, 723.

[9] D. Shahgholian-Ghahfarokhi, M. Safarpour, A. Rahimi, *Mech. Based Des. Struct. Mach.* **2021**, *49*, 81.

[10] C. Ma, S. Wu, Q. Ze, X. Kuang, R. Zhang, H. J. Qi, R. Zhao, *ACS Appl. Mater. Interfaces* **2021**, *13*, 12639.

[11] Y. Jiang, Z. Liu, N. Matsuhisa, D. Qi, W. R. Leow, H. Yang, J. Yu, G. Chen, Y. Liu, C. Wan, Z. Liu, X. Chen, *Adv. Mater.* **2018**, *30*, 1706589.

[12] Y. Cheng, X. Zhang, Y. Qin, P. Dong, W. Yao, J. Matz, P. M. Ajayan, J. Shen, M. Ye, *Nat. Commun.* **2021**, *12*, 1.

[13] E. Kim, H. Zhang, J. H. Lee, H. Chen, H. Zhang, M. H. Javed, X. Shen, J. K. Kim, *Compos. Part A Appl. Sci. Manuf.* **2021**, *147*, 106430.

[14] Q. Wang, Z. Li, Y. Zhang, S. Cui, Z. Yang, Z. Lu, *Compos. B Eng.* **2020**, *202*, 108379.

[15] M. T. Hsieh, C. S. Ha, Z. Xu, S. Kim, H. F. Wu, V. Kunc, X. Zheng, *J. Mater. Res.* **2021**, *36*, 3628.

[16] X. Fan, Q. Tang, Q. Feng, S. Ma, J. Song, M. Jin, F. Guo, P. Jin, *Int. J. Mech. Sci.* **2021**, *204*, 106586.

[17] X. Li, X. Yu, J. W. Chua, H. P. Lee, J. Ding, W. Zhai, *Small* **2021**, *17*, 2100336.

[18] S. Babaee, J. Shim, J. C. Weaver, E. R. Chen, N. Patel, K. Bertoldi, *Adv. Mater.* **2013**, *25*, 5044.

[19] Y. Chen, T. Li, F. Scarpa, L. Wang, *Phys. Rev. Appl.* **2017**, *7*, 024012.

[20] Y. Qin, Q. Peng, Y. Ding, Z. Lin, C. Wang, Y. Li, F. Xu, J. Li, Y. Yuan, X. He, Y. Li, *ACS Nano* **2015**, *9*, 8933.

[21] Q. Peng, Y. Qin, X. Zhao, X. Sun, Q. Chen, F. Xu, Z. Lin, Y. Yuan, Y. Li, J. Li, W. Yin, C. Gao, F. Zhang, X. He, Y. Li, *ACS Appl. Mater. Interfaces* **2017**, *9*, 44010.

[22] Y. Pang, H. Tian, L. Tao, Y. Li, X. Wang, N. Deng, Y. Yang, T. L. Ren, *ACS Appl. Mater. Interfaces* **2016**, *8*, 26458.

[23] B. Wicklein, A. Kocjan, G. Salazar-Alvarez, F. Carosio, G. Camino, M. Antonietti, L. Bergstrom, *Nat. Nanotechnol.* **2015**, *10*, 277.

[24] C. Wu, X. Huang, X. Wu, R. Qian, P. Jiang, *Adv. Mater.* **2013**, *25*, 5658.

[25] S. Zhao, Y. Zhang, Y. Zhang, J. Yang, S. Kitipornchaia, *Int. J. Mech. Sci.* **2021**, *212*, 106814.

[26] H. B. Zhang, Q. Yan, W. G. Zheng, Z. He, Z. Z. Yu, *ACS Appl. Mater. Interfaces* **2011**, *3*, 918.

[27] Q. Zhang, X. Xu, D. Lin, W. Chen, G. Xiong, Y. Yu, T. S. Fisher, H. Li, *Adv. Mater.* **2016**, *28*, 2229.

[28] K. Zhao, T. Zhang, H. Chang, Y. Yang, P. Xiao, H. Zhang, C. Li, C. S. Tiwary, P. M. Ajayan, Y. Chen, *Sci. Adv*. **2019**, *5*, eaav2589.

[29] J. J. Shang, Q. S. Yang, X. Liu, C. Wang, *Carbon* **2018**, *134*, 398.

[30] L. Valentini, S. B. Bon, N. M. Pugno, *Adv. Funct. Mater.* **2017**, *27*, 1606526.

[31] L. Lu, X. Chen, X. Huang, K. Lu, Science **2009**, *323*, 607.

[32] X. Huang, W. Xia, R. Zou, *J. Mater. Chem. A* **2014**, *2*, 19963.

[33] H. D. Baehr, Stephan K. *Heat and Mass Transfer* (2Ed.), Springer, Berlin Heidelberg **2014**.

[34] G. Bai, D. Gao, Z. Liu, X. Zhou, J. Wang, *Nature* **2019**, *576*, 437.

[35] F. Wu, A. Xie, M. Sun, Y. Wang, M. Wang, *J. Mater. Chem. A* **2015**, *3*, 14358.

[36] Q. Zhang, M. Hao, X. Xu, G. Xiong, H. Li, T. Fisher, *ACS Appl. Mater. Inter*. **2016**, *9*, 14232.

[37] C. Liu, H. Huang, Y. Wu, S. Fan. *Appl. Phys. Lett.* **2004**, *84*, 4248.

Table of Contents

A 3D graphene metamaterial with twin-structured morphology was constructed via orientated manipulation of icing growth and temperature gradient, which has demonstrated the anomalous physical properties such as programable Poisson's ratio, super-elasticity and high resilience. Both experimental investigation and numerical simulation have cooperatively validated the triggering mechanism depending on the oriented evolution of hierarchical microstructure and elastic buckling of the cell walls.

Zaishan Lin, Jiaqi Dong, Xin Wang, Qitao Huang, Xi Shen, Minglong Yang, Xianxian Sun, Ye Yuan, Shasha Wang, Yuanhao Ning, Shuang Yang, Weilong Yin, Menglin Li, and Qiangqiang Zhang*, Yibin Li*

Twin-structured Graphene Metamaterials with Anomalous Mechanical Properties